Supporting Information

Sequential Reinforcement of Intra/Interlayer Interfaces to Design Flexible, Transparent Electromagnetic Interference Shielding Film for "Green Electronics"

Gao Deng,[a] Xin Sun,[b] Xufeng Li,[a] Zhenyang Li,[a] Haihan Zou,[a] Peng Yi,[a] Ming Fang,[a] Chunyan Chen,[a] Junzhe He,[ab] Jianglan Shui,[a] Ronghai Yu*[a] and Xiaofang Liu*[a]

[a] *School of Materials Science and Engineering, Beihang University, Beijing, 100191, PR China*

[b] *Science and Technology on Electromagnetic Scattering Laboratory, Beijing Institute of Environmental Features, Beijing 100854, PR China*

[*] *Corresponding authors: Ronghai Yu (Email: rhyu@buaa.edu.cn), Xiaofang Liu (Email: liuxf05@buaa.edu.cn)*

Supplementary Information contains:

1. Supplementary Fig. S1−S21
2. Supplementary Table S1-S4
3. Supplementary References

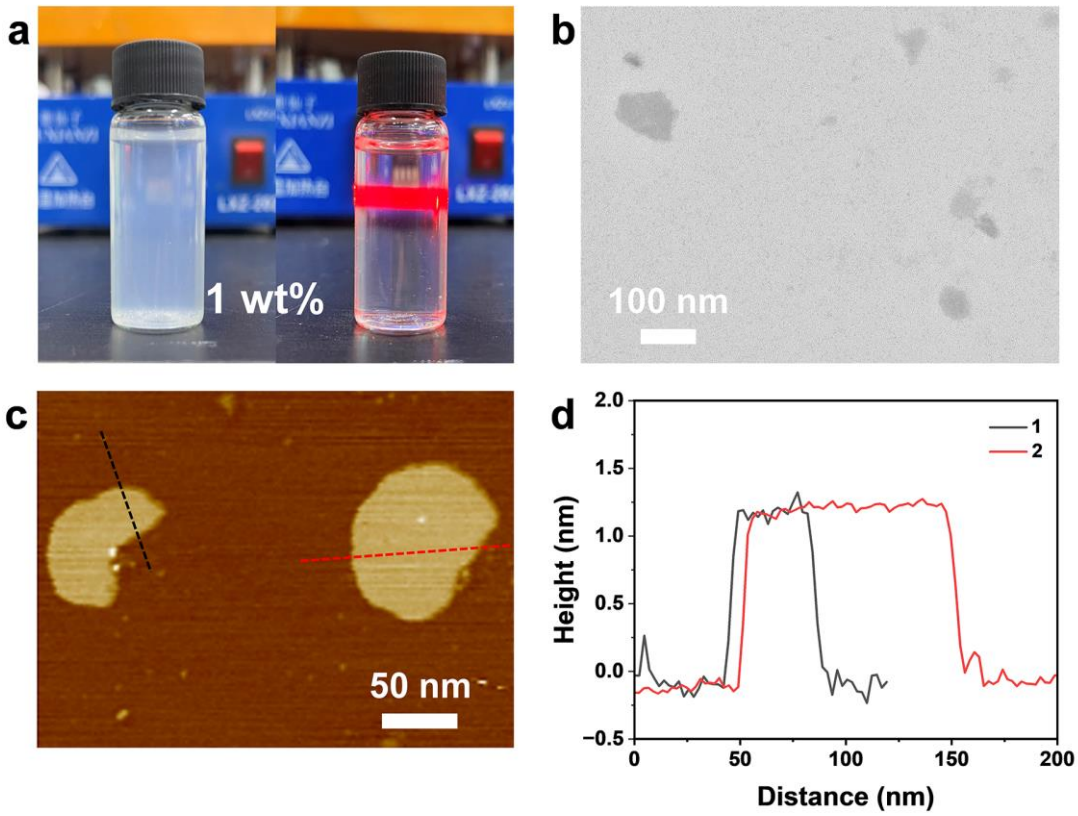

Fig. S1 (a) Digital photo of nanoclay dispersion before (left) and after (right) exfoliation. (b) TEM image, (c) AFM image, and (d) height profile of exfoliated nanoclay platelets.

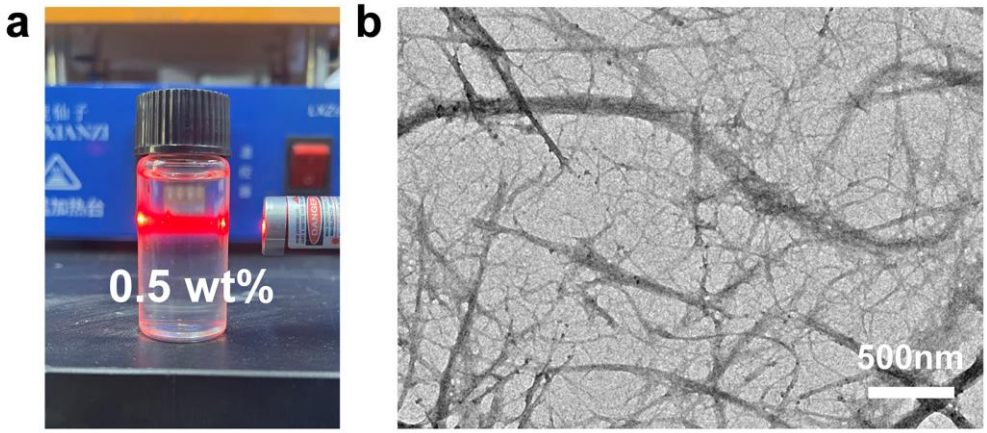

Fig. S2 (a) Digital photo of CNF dispersion. (b) TEM image of TEMPO-oxidized CNFs.

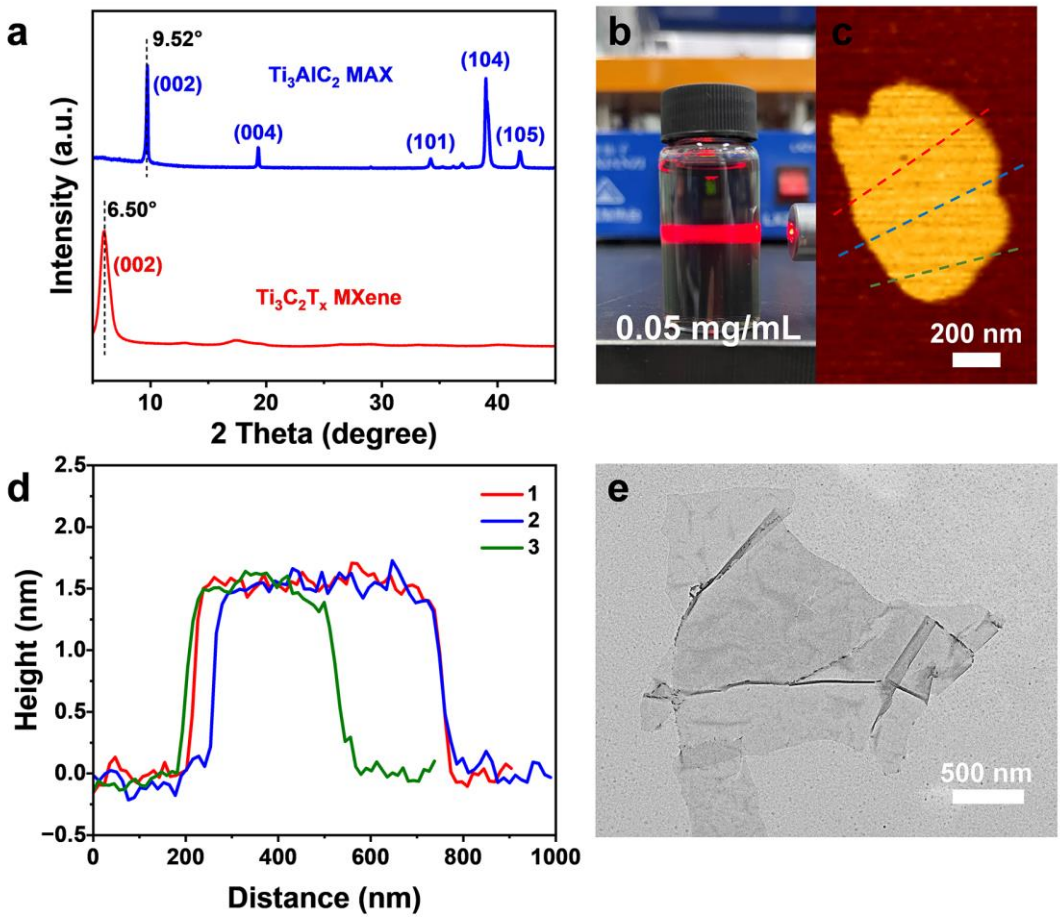

Fig. S3 (a) XRD patterns of MXene nanosheets and Ti_3AlC_2 powder. (b) Digital photo of MXene dispersion. (c) AFM image, (d) height profile, and (e) TEM image of MXene nanosheet.

As shown in the XRD patterns, the characteristic peaks of MAX powders at 39.17° disappear after exfoliation. The (002) diffraction peak shifts from 9.52° towards 6.50°, which is attributed to the increased interlayer spacing. These results reveal the successful exfoliation of MXene nanosheets.

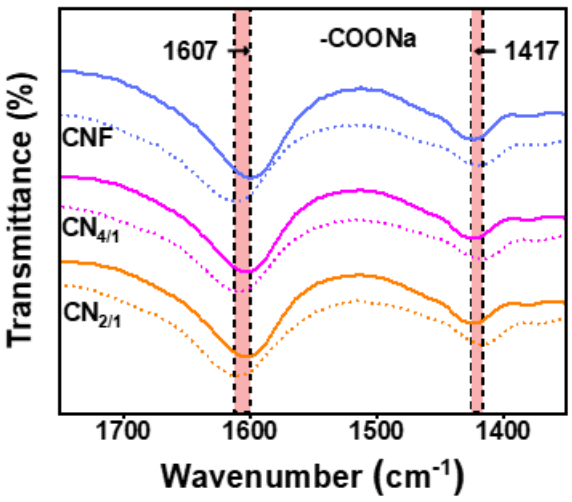

Fig. S4 FTIR spectra of CNF, $CN_{4/1}$, $CN_{2/1}$ films with Ca^{2+} (solid lines) and without Ca^{2+} (dotted lines).

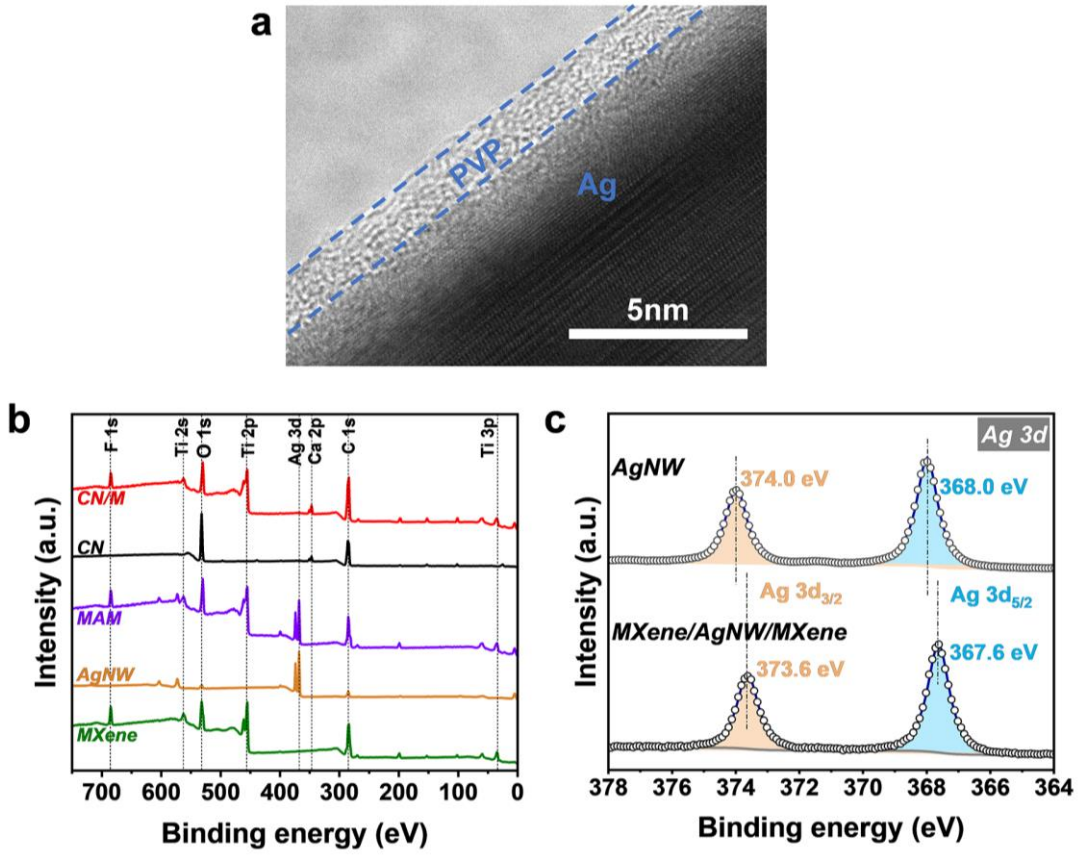

Fig. S5 (a) High-resolution TEM image of AgNW. (b) XPS survey spectra of different films. (c) High-resolution Ag 3d XPS spectra of AgNWs and MXene/AgNW/MXene film.

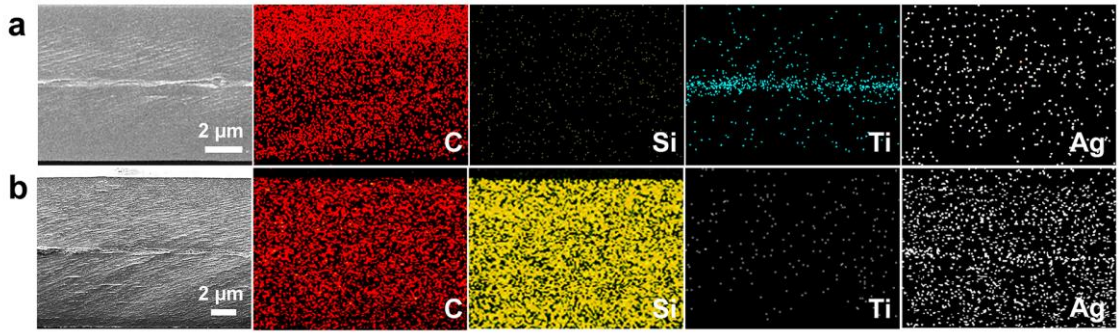

Fig. S6 SEM images and corresponding EDS elemental mappings of the cross-sections of (a) C/MAM/C and (b) $CN_{2/1}$/A/$CN_{2/1}$ films.

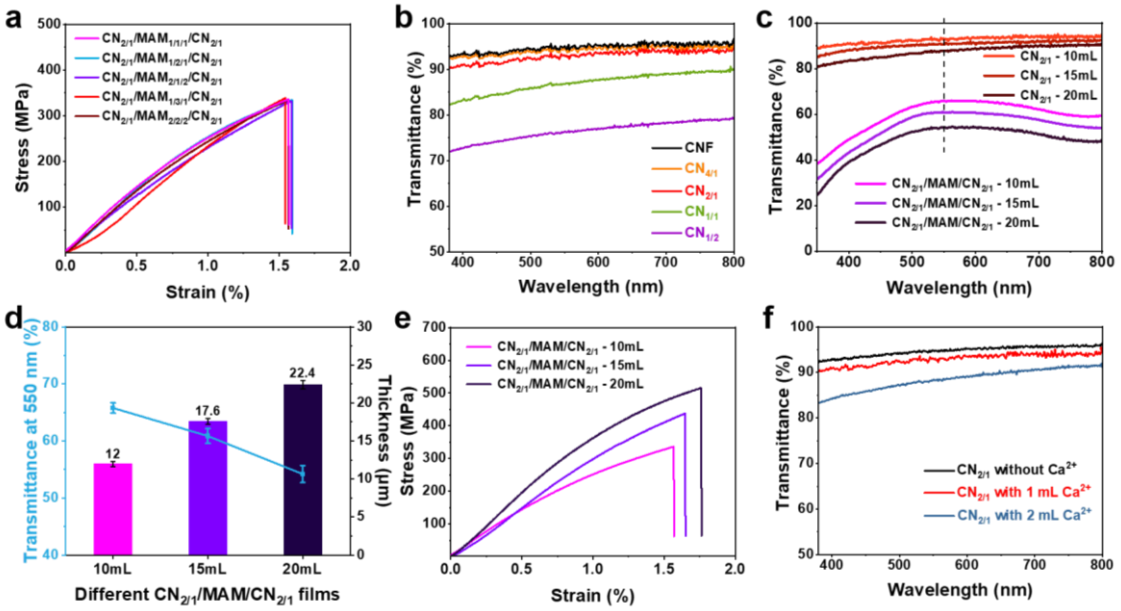

Fig. S7 (a) Stress-strain curves of different $CN_{2/1}/MAM_{\alpha/\beta/\alpha}/CN_{2/1}$ films. (b) Visible-light transmittance curves of $CN_{x/y}$ films with different component ratios. (c) Visible-light transmittance curves, (d) thickness and optical transmittance at 550 nm wavelength, and (e) stress-strain curves of $CN_{2/1}/MAM/CN_{2/1}$ films with different substrate thickness. (f) Visible-light transmittance curves of $CN_{2/1}$ films with different amounts of Ca^{2+}.

For Fig. S7c-e, the composite films were prepared using different amounts of CN suspension. In experiment, we fixed the compositions of substrate ($CN_{2/1}$) and conductive layer ($MAM_{1/1/1}$), and prepared three films with the CN suspensions of 10, 15 and 20 ml, respectively. As the thickness of substrate increases, the tensile strength and elongation at break of composite film increase, while the transmittance decreases. Therefore, the optimal thickness of the substrate should be the thinnest among the three samples (i.e. CN suspension of 10 ml).

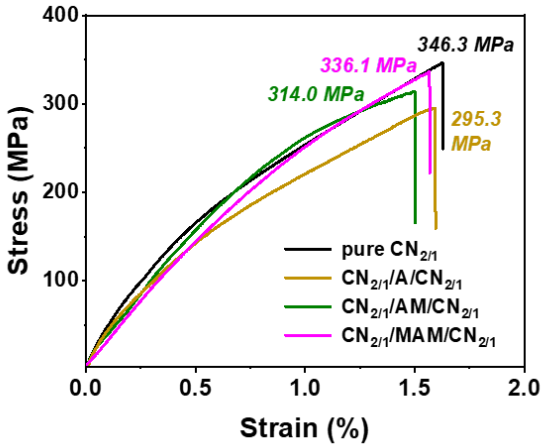

Fig. S8 Stress-strain curves of pure $CN_{2/1}$, $CN_{2/1}$/A/$CN_{2/1}$, $CN_{2/1}$/AM/$CN_{2/1}$ and $CN_{2/1}$/MAM/$CN_{2/1}$.

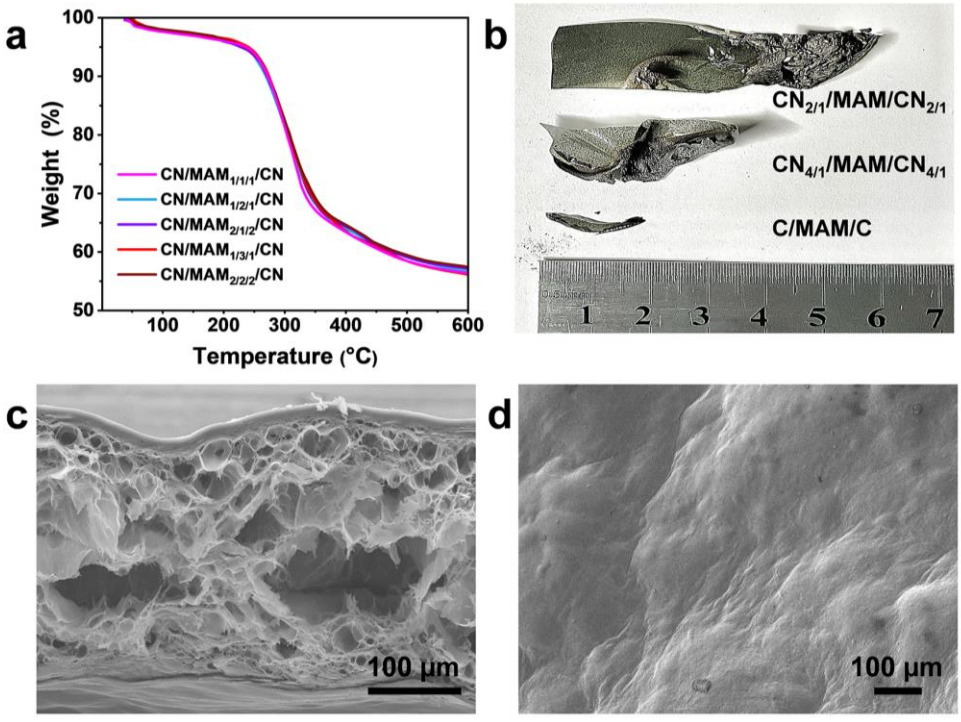

Fig. S9 (a) TGA curves of different $CN_{2/1}$/$MAM_{\alpha/\beta/\alpha}$/$CN_{2/1}$ films measured under nitrogen atmosphere. (b) Digital photos of the residues of different films after vertical flame combustion test. (c, d) SEM images of the cross-section and surface of $CN_{2/1}$/MAM/$CN_{2/1}$ residue.

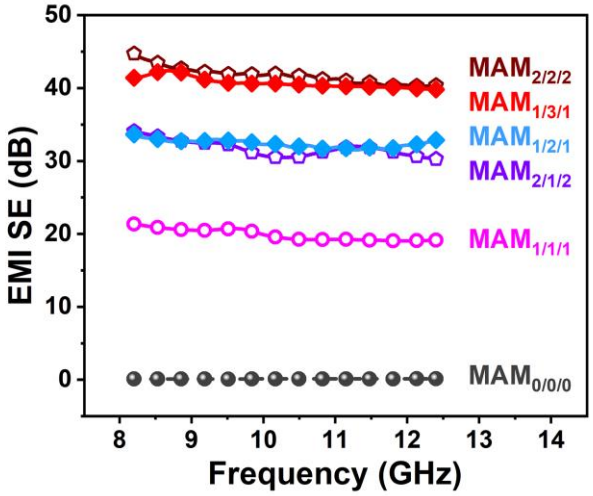

Fig. S10 EMI SE curves of different CN/MAM$_{\alpha/\beta/\alpha}$/CN films.

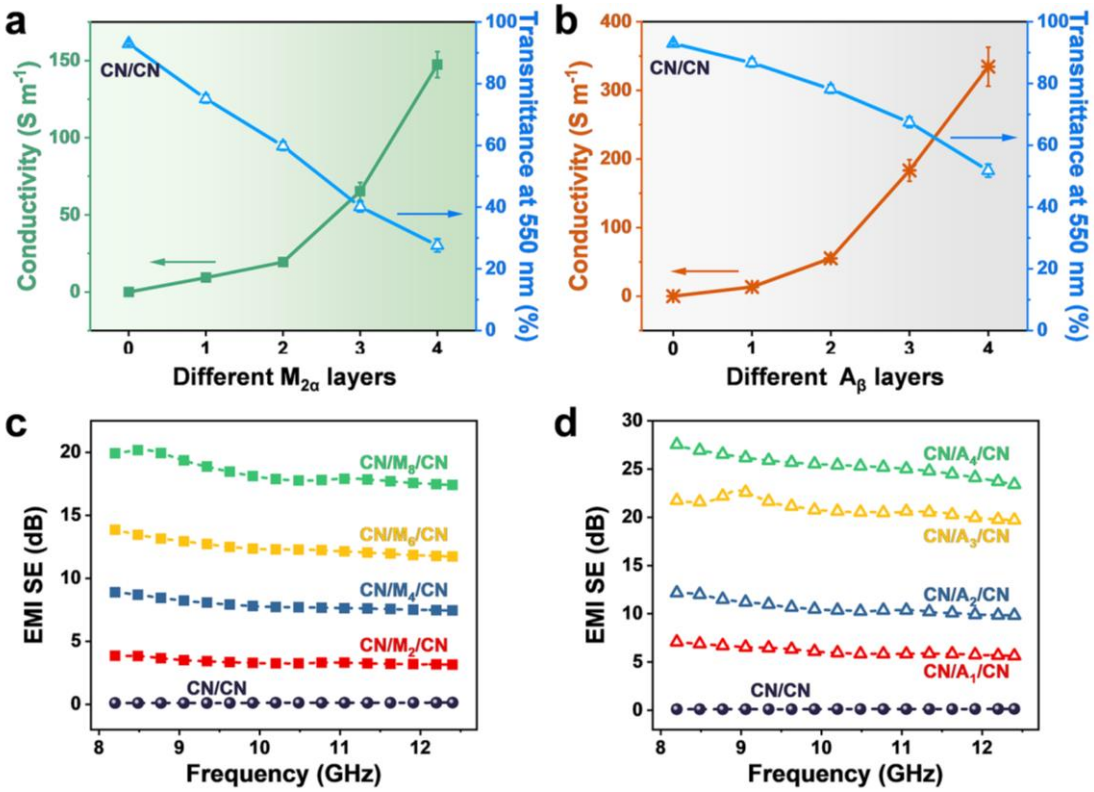

Fig. S11 (a) Conductivity of $M_{2\alpha}$ layers and optical transmittance at 550 nm of CN/$M_{2\alpha}$/CN films. (b) Conductivity of A_β layers and optical transmittance at 550 nm of CN/A_β/CN films. (c) EMI SE curves of CN/$M_{2\alpha}$/CN films. (d) EMI SE curves of CN/A_β/CN films.

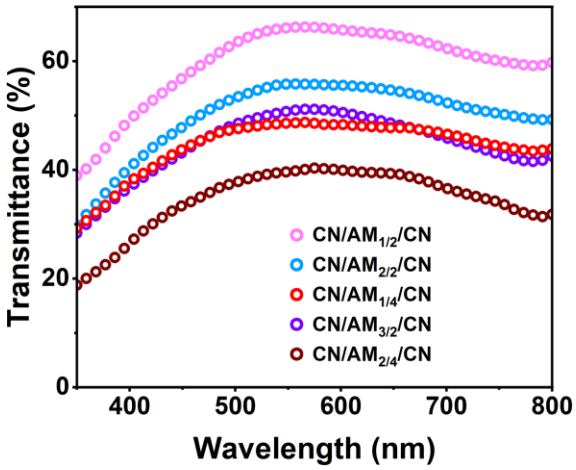

Fig. S12 Optical transmittance curves of CN/AM$_{\beta/2\alpha}$/CN films.

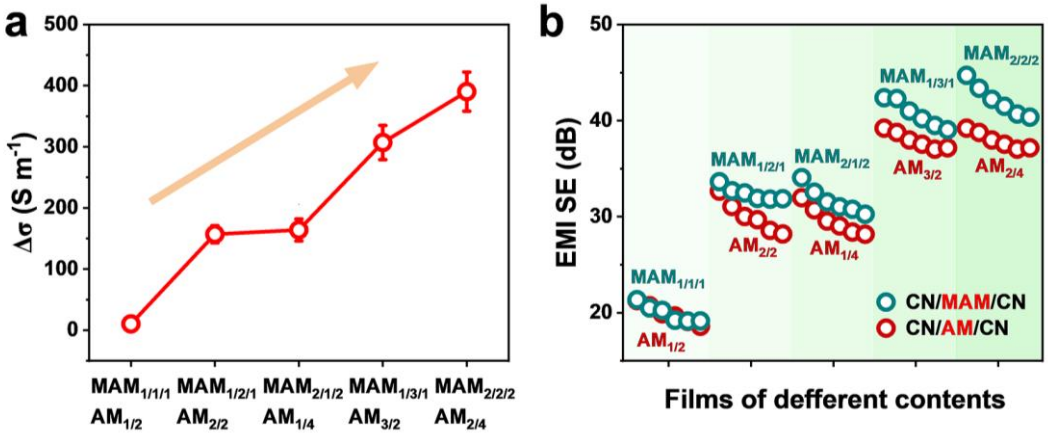

Fig. S13 (a) Difference in conductivity $\Delta\sigma$ [i.e. $\sigma_{(MAM)}$ - $\sigma_{(AM)}$] between the two conductive layers. (b) EMI SE of CN/MAM$_{\alpha/\beta/\alpha}$/CN and CN/AM$_{\beta/2\alpha}$/CN films.

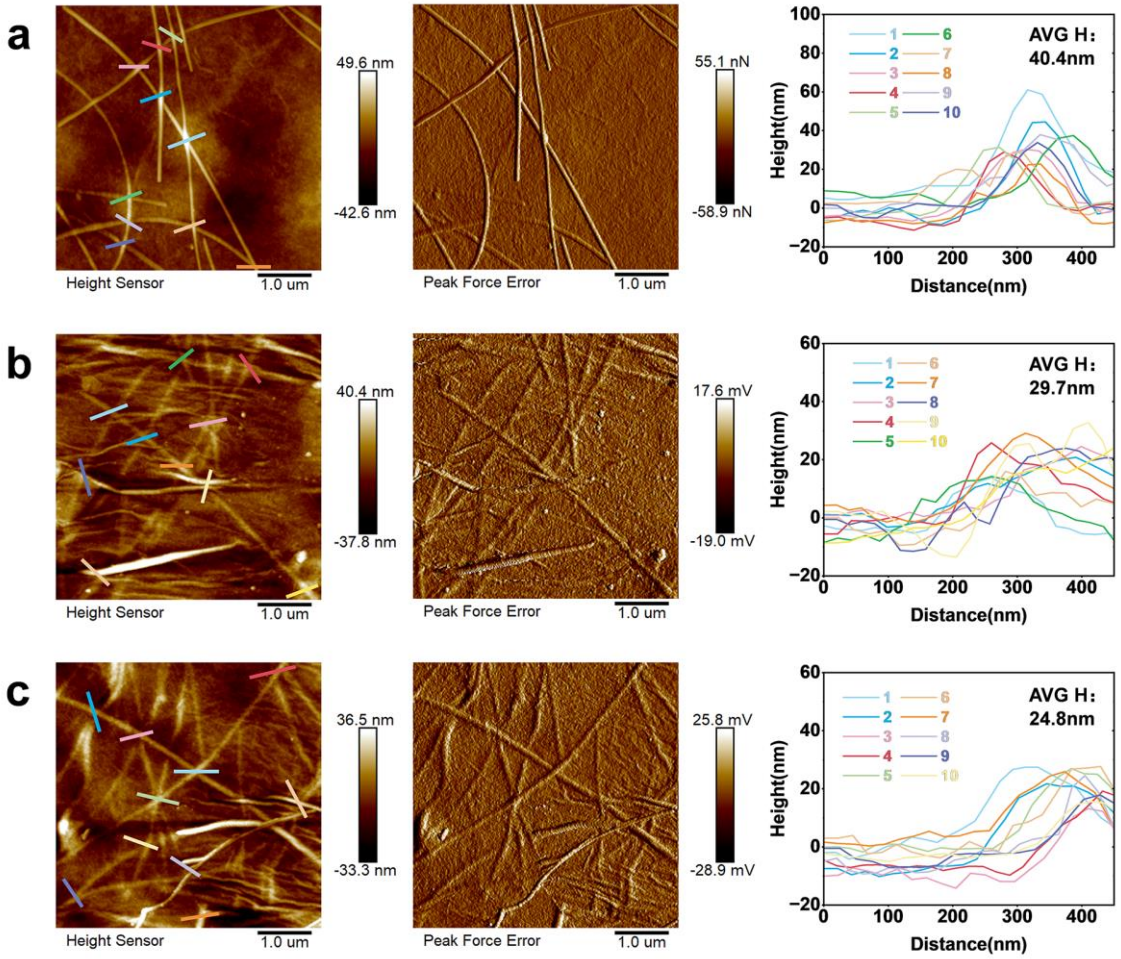

Fig. S14 AFM images and height statistics of AgNW junctions in (a) CN/A_1 film, (b) CN/$AM_{1/2}$ film, and (c) CN/$MAM_{1/1/1}$ film.

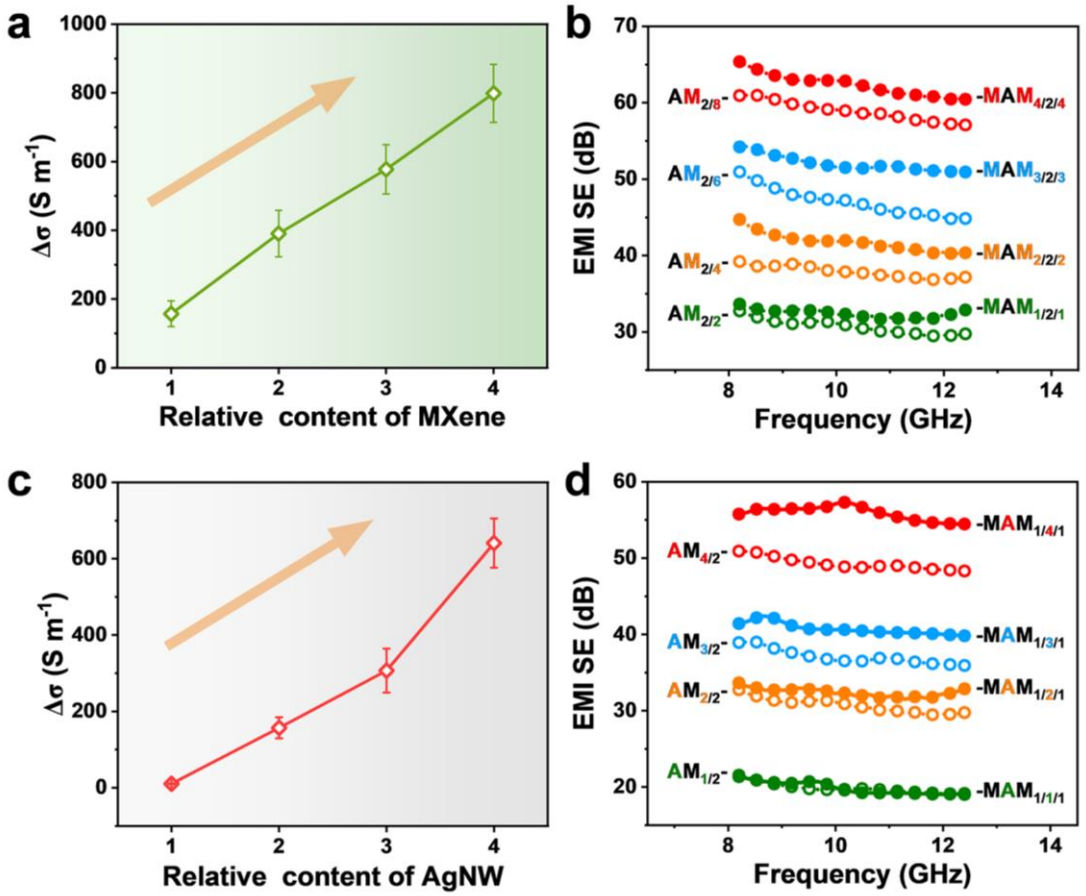

Fig. S15 (a) Conductivity difference $\Delta\sigma$ between $AM_{2/2\alpha}$ and $MAM_{\alpha/2/\alpha}$ conductive layers. Ag content β is fixed at 2 and MXene content 2α increases from 1 to 4. (b) EMI SE curves of $CN/AM_{2/2\alpha}/CN$ and $CN/MAM_{\alpha/2/\alpha}/CN$ films. Ag content β is fixed at 2 and MXene content 2α increases from 1 to 4. (c) Conductivity difference $\Delta\sigma$ between $AM_{\beta/2}$ and $MAM_{1/\beta/1}$ conductive layers. MXene content 2α is fixed at 2 and Ag content β increases from 1 to 4. (d) EMI SE curves of $CN/AM_{\beta/2}/CN$ and $CN/MAM_{1/\beta/1}/CN$ films. MXene content 2α is fixed at 2 and Ag content β increases from 1 to 4.

At a fixed Ag content, the continuous increase in $\Delta\sigma$ and ΔSE demonstrates the enhanced welding effect by more MXene (Fig S15a-b). Similarly, at a fixed MXene content, both $\Delta\sigma$ and ΔSE increases with Ag nanowire junctions, indicating that more Ag nanowire junctions are well-welded (Fig S15c-d).

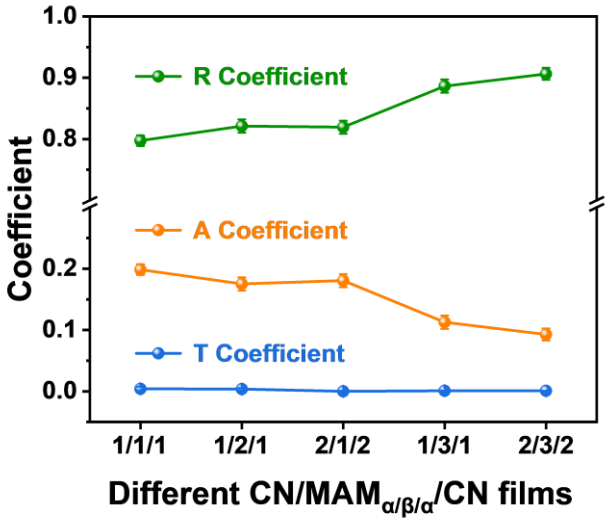

Fig. S16 The average A, R and T power coefficients of different CN/MAM$_{\alpha/\beta/\alpha}$/CN films.

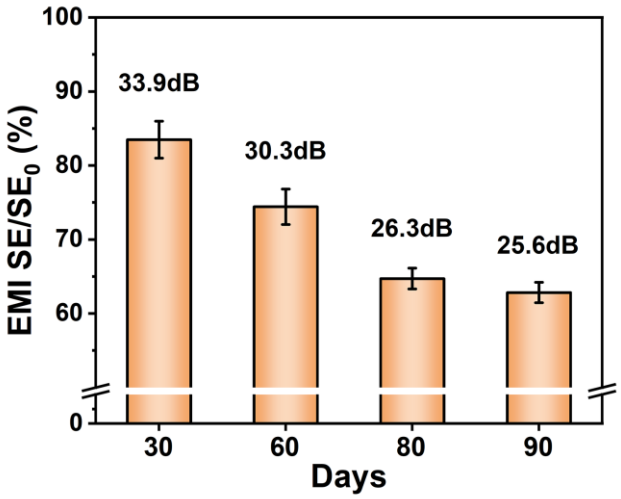

Fig. S17 Retention rates of the average SE values of CN/MAM$_{1/3/1}$ film after 30, 60, 80 and 90 days.

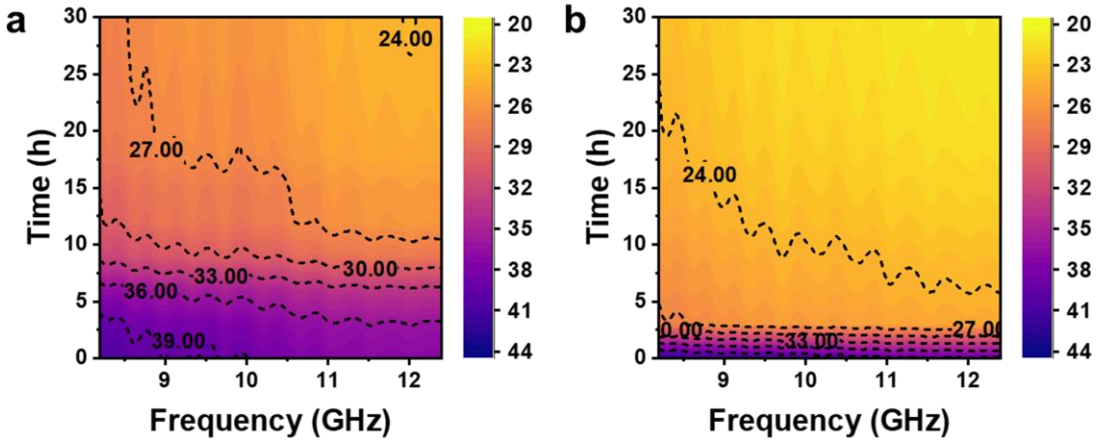

Fig. S18 3D projection of EMI SE curves of (a) CN/$MAM_{1/3/1}$/CN and (b) CN/$MAM_{1/3/1}$ films heated at 200 °C for 30 h.

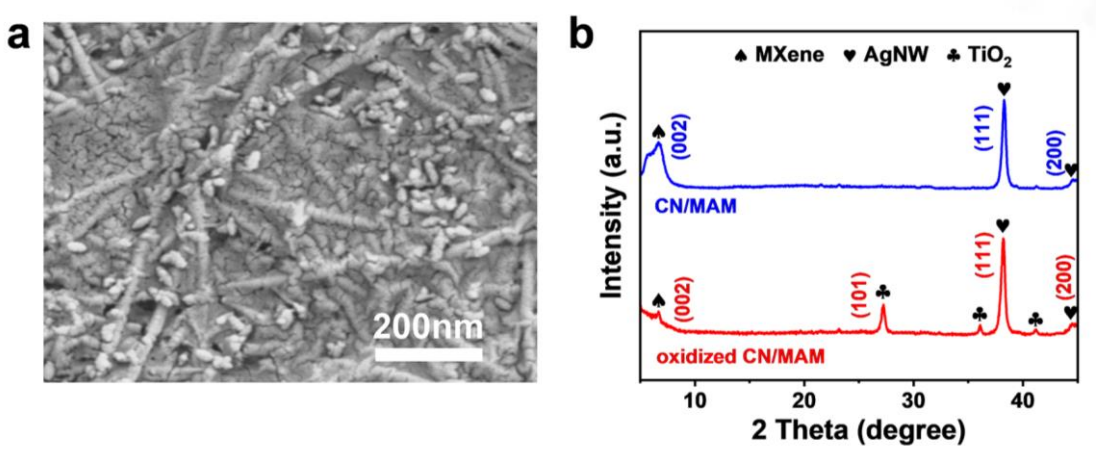

Fig. S19 (a) SEM image of CN/$MAM_{1/3/1}$ film after heating at 200 °C for 3 h. (b) XRD patterns of the pristine CN/$MAM_{1/3/1}$ film and the CN/$MAM_{1/3/1}$ film after heating at 200 °C for 3 h.

Fig. S19a shows the formation of TiO_2 nanoparticles on MXene sheets after heating at 200 °C for 3 h. Compared with the XRD pattern of pristine CN/$MAM_{1/3/1}$ film, a clear diffraction peak of TiO_2 appears in the XRD pattern after heating at 200 °C for 3 h.

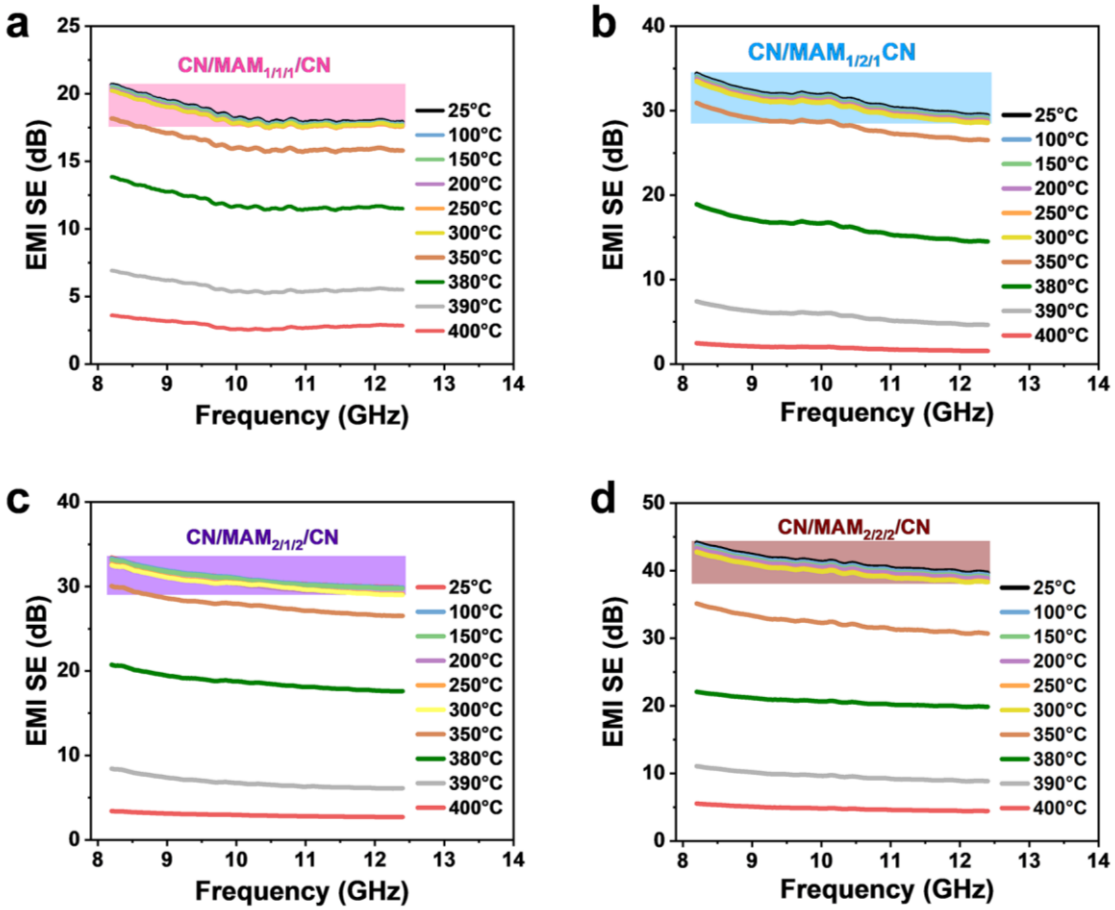

Fig. S20 EMI SE curves of (a) CN/MAM$_{1/1/1}$/CN, (b) CN/MAM$_{1/2/1}$/CN, (c) CN/MAM$_{2/1/2}$/CN, and (d) CN/MAM$_{2/2/2}$/CN films from room temperature to 400 °C.

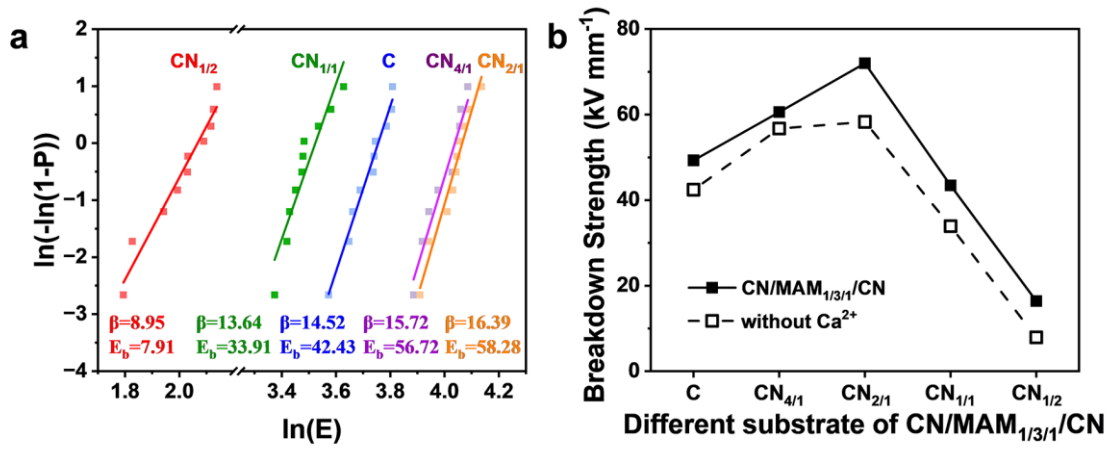

Fig. S21 (a) Weibull plots and (b) breakdown strength E_b of $CN_{x/y}$/MAM/$CN_{x/y}$ films without Ca^{2+}.

The two-parameter statistics, Weibull distribution, is widely used to evaluate the probability of breakdown:[1]

$$P(E) = 1 - exp\,[-(E/E_b)^{\beta}] \quad \text{(S1)}$$

where $P(E)$ is the cumulative probability of electric breakdown failure, E is the tested breakdown strength, E_b is the standard breakdown strength of the material when the cumulative probability is 63.2%, and β is the shape parameter. Generally, the larger β value, the higher the stability of the material breakdown. To obtain E_b and β values, we can take the logarithm of both sides of Equation (S1), and then get a simple linear function:

$$\ln[-\ln(1-P)] = \beta(\ln E - \ln E_b) \quad \text{(S2)}$$

Moreover, the empirical distribution function is obtained by the Bernard's median rank estimator formula:[2]

$$P_i(E) = (i - 0.3)/(n + 0.4) \quad \text{(S3)}$$

where i refers to the order of tested breakdown strength from smallest to largest, n is the total number of the sample tested.

Table S1 Oxygen transmission rate (OTR, $cm^3\ m^{-2}\ d^{-1}\ atm^{-1}$) and oxygen permeability (OP, $cm^3\ \mu m\ m^{-2}\ d^{-1}\ atm^{-1}$) of composite films.

Samples	Average thickness (μm)	45%RH OTR ($cm^3\ m^{-2}\ d^{-1}\ atm^{-1}$)	45%RH OP ($cm^3\ \mu m\ m^{-2}\ d^{-1}\ atm^{-1}$)	95%RH OTR ($cm^3\ m^{-2}\ d^{-1}\ atm^{-1}$)	95%RH OP ($cm^3\ \mu m\ m^{-2}\ d^{-1}\ atm^{-1}$)
C/MAM/C	8±0.23	16.09	128.72	1425.48	11403.84
$CN_{4/1}$/MAM/$CN_{4/1}$	10±0.35	0.1431	1.431	216.71	2167.1
$CN_{2/1}$/MAM/$CN_{2/1}$	12±0.34	0.04897	0.5876	17.52	210.24
$CN_{1/1}$/MAM/$CN_{1/1}$	13±0.28	0.04952	0.6438	13.575	176.47
$CN_{1/2}$/MAM/$CN_{1/2}$	14±0.32	0.07443	1.042	12.02	168.28
$CN_{2/1}$/MAM/$CN_{2/1}$-without Ca^{2+}	12±0.51	0.05262	0.6314	23.14	277.68
$CN_{2/1}$/$MAM_{1/3/1}$/$CN_{2/1}$	12.1±0.27	0.04643	0.5618	17.83	215.74

Table S2 Flammability data of composite films.

Samples	Weight (g)	Afterglow time (s)[a]	Residue (%)	Damaged length (mm)	Limiting oxygen index (%)
C/MAM/C	0.105	9.5	<1	~80	20.6
$CN_{4/1}$/MAM/$CN_{4/1}$	0.121	6.0	41	~62	44.1
$CN_{2/1}$/MAM/$CN_{2/1}$	0.134	0.1	84	~41	74.5

[a] Afterglow time refers to the time of continuous flameless combustion.

Table S3 Characteristic parameters of microscale combustion calorimetry of composite films.

Samples	PHRR (W g^{-1})[a]	THR (kJ g^{-1})[b]	T_{PHRR} (°C)[c]
C/MAM/C	117.3	3.8	277.7
$CN_{4/1}$/MAM/$CN_{4/1}$	57.1	2.1	280.2
$CN_{2/1}$/MAM/$CN_{2/1}$	40.1	1.2	287.3

[a] PHRR refers to the peak heat release rate; [b] THR refers to the total heat released; [c] T_{PHRR} refers to the peak temperature of peak heat release rate.

Table S4 Comparison of the SE/t values of transparent/translucent flexible EMI shielding films.

	Materials	Substrate	Thickness (μm)	EMI SE (dB)	SE/t (dB cm^{-1})	Ref
AgNW-based	AgNW	PMMA	250	33	1320.0	3
	Fe_3O_4/AgNW	PET	50	26.2	5240.0	4
	AgNF	PET	120	58	4833.3	5
	AgNW	Gelatin	27	37.74	13977.8	6
	AgNW	Glass	50	31.3	6260.0	7
	AgNW	SA	25	27.9	11160.0	8
	AgNW	PET	150	29	1933.3	9
	AgNW	Cellulose	145	39	2696.6	10
Carbon-based	RGO/AgNW	PET	100	30	3000	11
	GNS/AgNW	-	30	38	12666.7	12
	RGO	PEI	4	6.37	15925.0	13
MXene-based	MXene/AgNW	PET	125	23.7	1896.0	14
	MXene-SWCNT	Glass	1000	3.3	33	15
	MXene/AgNW	PU	450	32.5	722.2	16
	MXene/AgNW	PET	125	27.1	2168	17
	MXene/AgNW	PET	100	32.5	3250	18
This work	CN/$MAM_{1/1/1}$/CN	Cellulose/ Nanoclay	12	19.9	16583.3	
	CN/$MAM_{1/2/1}$/CN			32.4	27000.0	
	CN/$MAM_{2/1/2}$/CN			31.7	26416.6	
	CN/$MAM_{1/3/1}$/CN			40.7	33916.6	
	CN/$MAM_{2/2/2}$/CN			41.7	34750.0	

Supplementary references

1. B. C. Luo, Z. H. Shen, Z. M. Cai, E. K. Tian, Y. Yao, B. W. Li, A. Kursumovic, J. L. MacManus-Driscoll, L. T. Li, L. Q. Chen and X. H. Wang, *Adv. Funct. Mater.*, 2021, **31**, 11.
2. L. F. Zhang, M. Xie and L. C. Tang, *Qual. Reliab. Eng. Int.*, 2006, **22**, 905-917.
3. X. Zhang, Y. L. Zhong and Y. Yan, *Phys. Status Solidi A-Appl. Mat.*, 2018, **215**, 5.
4. Z. X. Wang, B. Jiao, Y. C. Qing, H. Y. Nan, L. Q. Huang, W. Wei, Y. Peng, F. Yuan, H. Dong, X. Hou and Z. X. Wu, *ACS Appl. Mater. Interfaces*, 2020, **12**, 2826-2834.
5. S. Lin, H. Y. Wang, F. Wu, Q. M. Wang, X. P. Bai, D. Zu, J. N. Song, D. Wang, Z. L. Liu, Z. W. Li, N. Tao, K. Huang, M. Lei, B. Li and H. Wu, *npj Flex. Electron.*, 2019, **3**, 8.
6. G. H. Wang, L. L. Hao, X. D. Zhang, S. J. Tan, M. Zhou, W. H. Gu and G. B. Ji, *J. Colloid Interface Sci.*, 2022, **607**, 89-99.
7. X. Z. Zhu, J. Xu, F. Qin, Z. Y. Yan, A. Q. Guo and C. X. Kan, *Nanoscale*, 2020, **12**, 14589-14597.
8. H. J. Wang, J. H. Guo, Y. T. Lei, W. Y. Chen, Z. C. Zhang, M. Zhu and H. L. Xu, *ACS Appl. Nano Mater.*, 2024, **7**, 2100-2109.
9. X. Z. Zhu, A. Q. Guo, Z. Y. Yan, F. Qin, J. Xu, Y. D. Ji and C. X. Kan, *Nanoscale*, 2021, **13**, 8067-8076.
10. M. Zhu, X. X. Yan, X. Li, L. Dai, J. H. Guo, Y. T. Lei, Y. J. Xu and H. L. Xu, *ACS Appl. Mater. Interfaces*, 2022, **14**, 45697–4570610.
11. D. G. Kim, J. H. Choi, D. K. Choi and S. W. Kim, *ACS Appl. Mater. Interfaces*, 2018, **10**, 29730-29740.
12. N. Zhang, Z. Wang, R. G. Song, Q. L. Wang, H. Y. Chen, B. Zhang, H. F. Lv, Z. Wu and D. P. He, *Sci. Bull.*, 2019, **64**, 540-546.
13. S. Kim, J. S. Oh, M. G. Kim, W. Jang, M. Wang, Y. Kim, H. W. Seo, Y. C. Kim, J. H. Lee, Y. Lee and J. D. Nam, *ACS Appl. Mater. Interfaces*, 2014, **6**, 17647-17653.
14. W. Chen, L. X. Liu, H. B. Zhang and Z. Z. Yu, *ACS Nano*, 2020, **14**, 16643-16653.
15. G. M. Weng, J. Y. Li, M. Alhabeb, C. Karpovich, H. Wang, J. Lipton, K. Maleski, J. Kong, E. Shaulsky, M. Elimelech, Y. Gogotsi and A. D. Taylor, *Adv. Funct. Mater.*, 2018, **28**, 9.
16. Z. C. Wang, P. Wang, W. X. Cao, C. Q. Sun, Z. C. Song, D. C. Ji, L. Yang, J. C. Han and J. Q. Zhu, *J. Mater. Chem. C*, 2022, **10**, 17066-17074.
17. Y. S. Zhang, T. Wang, Z. L. Bao, P. F. Qian, X. C. Liu, W. H. Geng, D. Zhang, S. W. Wang, Q. X. Zhu and H. Z. Geng, *J. Colloid Interface Sci.*, 2024, **665**, 376-388.
18. M. Jin, W. Chen, L. X. Liu, H. B. Zhang, L. X. Ye, P. Min and Z. Z. Yu, *J. Mater. Chem. A*, 2022, **10**, 14364-14373.